Improved *ab initio* calculation of surface second-harmonic generation from Si(111)(1×1):H

Sean M. Anderson,[1] Nicolas Tancogne-Dejean,[2,3,4] Bernardo S. Mendoza,[1,*] and Valérie Véniard[2,4]

[1]*Centro de Investigaciones en Óptica, León, Guanajuato, México*
[2]*Laboratoire des Solides Irradiés, École Polytechnique, Centre National de la Recherche Scientifique, CEA/DSM, 91128 Palaiseau, France*
[3]*Max Planck Institute for the Structure and Dynamics of Matter, Luruper Chaussee 149, D-22761 Hamburg, Germany*
[4]*European Theoretical Spectroscopy Facility, Palaiseau, France*

We carry out an improved *ab initio* calculation of surface second-harmonic generation (SSHG) from the Si(111)(1×1):H surface. This calculation includes three new features in one formulation: (i) the scissors correction, (ii) the contribution of the nonlocal part of the pseudopotentials, and (iii) the inclusion of a cut function to extract the surface response, all within the independent particle approximation. We apply these improvements on the Si(111)(1×1):H surface and compare with various experimental spectra from several different sources. We also revisit the three-layer model for the SSHG yield and demonstrate that it provides more accurate results over several, more common, two-layer models. We demonstrate the importance of using properly relaxed coordinates for the theoretical calculations. We conclude that this approach to the calculation of the second-harmonic spectra is versatile and accurate within this level of approximation. This well-characterized surface offers an excellent platform for comparison with theory and allows us to offer this study as an efficient benchmark for this type of calculation.

I. INTRODUCTION

Surface second-harmonic generation (SSHG) has been shown to be an effective, nondestructive, and noninvasive probe to study surface and interface properties [1–10]. SSHG experiments are now very cost effective and popular because they provide easy access to buried interfaces and nanostructures, and interest in these techniques continues to increase with the advent of ultrathin and bidimensional materials [11,12]. The high surface sensitivity of SSHG spectroscopy is due to the fact that within the dipole approximation the bulk second-harmonic generation in centrosymmetric materials is identically zero. The SHG process can occur only at the surface where the inversion symmetry is broken.

There are several theoretical formalisms that describe the SHG process for surfaces with different approximations and varying levels of difficulty [9,13–19]. In this paper, we focus on a recent approach developed by us in Ref. [20]. It includes three features not previously found in a single formulation: (i) the scissors correction, (ii) the contribution of the nonlocal part of the pseudopotentials, and (iii) the cut function used to extract the surface response, all within the independent particle approximation. The inclusion of these three contributions opens the possibility to study SSHG with more versatility and accuracy than was previously available at this level of approximation. We also use the three-layer model for the SSHG yield, which considers that the SH conversion takes place in a thin layer just below the surface that lies under the vacuum region and above the bulk of the material. Validating these improvements is difficult, however, without experimental data for comparison.

SSHG experiments focusing on semiconductor surfaces are available, but they are often reported over very limited energy ranges and lacking units and scale for the intensity.

This lack of comprehensive experimental data has made comparison between theory and experiment difficult. However, the Si(111)(1×1):H surface offers some respite in this area. This surface can be prepared to a high degree of structural quality and has been experimentally characterized with SHG to a great degree of accuracy [16,21]. The added H saturates the surface Si dangling bonds and eliminates any surface-related electronic states in the band gap. We consider that this surface represents an ideal benchmark for *ab initio* SSHG studies. More specifically, SSHG from the Si(111)(1×1):H surface was treated in detail in Ref. [16], and their approach yielded good qualitative results. However, the expressions presented for the nonlinear susceptibility tensor, $\chi(-2\omega;\omega,\omega)$, which is required for the SSHG yield, are derived in the velocity gauge. This method incorrectly implements the scissors quasiparticle correction and diverges for low energies [22]. They also propose a two-layer model for SSHG which does not accurately represent the real physical process for surfaces. We consider that the theoretical and computational aspects of this subject have evolved considerably since then, making this topic ripe for revision.

In this paper, we present a comparison between theory and experiment by presenting the improved theoretical calculations against experimental SSHG spectra from several sources, namely, Refs. [16,21,23,24], with two-photon energies ranging from 2.5 to 5 eV covering both the E_1 and E_2 critical point transitions for bulk Si. These SHG experiments were carried out with different polarizations of incoming and outgoing beams which are taken into account in the theoretical analysis. We find that the formalism compares favorably with experiment and permits insight into the physics behind SSHG. In spite of the advances mentioned, our treatment neglects local field and excitonic effects that are challenging from both a theoretical and a computational standpoint. This topic merits further review and may prove to be crucial for more accurate SSHG theory.

*bms@cio.mx

This paper is organized as follows. In Sec. II, we present the relevant equations and theory that describe the SSHG yield. In Sec. III, we present the components of the nonlinear second-order susceptibility tensor, $\chi(-2\omega;\omega,\omega)$, which are needed to calculate the SSHG yield. We describe our methodology and final parameters for these calculations in Sec. IV. In Sec. V, we show the results of the comparison between our improved formalism with the experimental spectra for the Si(111)(1×1):H surface. Finally, in Sec. VI, we present our conclusions and final remarks.

II. SSHG YIELD

We will briefly describe the three-layer model for the SSHG yield in this section. We mention that the formulas presented in Ref. [16], where the three-layer model was introduced for the first time, have some minor mistakes that have been corrected in Ref. [25]. These revised formulas are what we use in this paper and are presented below. We assume that the fundamental electric field at 1ω induces the second-harmonic conversion in a thin layer just below the surface described by a surface dielectric function, $\epsilon_\ell(\omega)$. This layer is below the vacuum region and above the material bulk that is described by the bulk dielectric function, $\epsilon_b(\omega)$, as depicted in Fig. 1. In this surface layer, the nonlinear polarization

$$\mathcal{P}^a(2\omega) = \chi^{abc}(-2\omega;\omega,\omega)E^b(\omega)E^c(\omega) \tag{1}$$

produces the SSHG that radiates into the vacuum where the measurements take place. In Eq. (1), $\mathbf{E}(\omega)$ is the fundamental electric field, and there is a sum over the repeated Cartesian indices. In this model, the SSHG yield is given by [25]

$$\mathcal{R}_{iF} = \frac{\omega^2}{2\epsilon_0 c^3 \cos^2\theta} \left| \Gamma_{iF}^\ell \, r_{iF}^\ell \right|^2, \tag{2}$$

where θ is the angle of incidence, c is the speed of light, and ϵ_0 is the vacuum permittivity. The i subscript denotes the incoming 1ω photon polarization and can be either p or s. Analogously, the F subscript is the polarization of the outgoing 2ω photon, which we represent with capital letters as either P or S. Equation (2) is written in the meter-kilogram-second (MKS) system of units, although the calculated SSHG yield is reported in cm^2/W.

FIG. 1. Representation of the three-layer model for SSHG. Vacuum is on top with $\varepsilon_v = 1$; the layer with nonlinear polarization $\mathcal{P}^a(2\omega) = \chi^{abc}(-2\omega;\omega,\omega)E^b(\omega)E^c(\omega)$ is characterized with $\varepsilon_\ell(\omega)$ and the bulk is characterized with $\varepsilon_b(\omega)$. In the dipole approximation, the bulk does not radiate second harmonic.

The Γ_{iF}^ℓ term contains the Fresnel factors for each polarization case, and they are given by

$$\Gamma_{pP}^\ell = \frac{T_p^{v\ell}(\omega)T_p^{\ell b}(\omega)}{\sqrt{\varepsilon_\ell(\omega)}\varepsilon_\ell(2\omega)\sqrt{\varepsilon_b(2\omega)}} \left[\frac{t_p^{v\ell}(\omega)t_p^{\ell b}(\omega)}{\varepsilon_\ell(\omega)\sqrt{\varepsilon_b(\omega)}} \right]^2,$$

$$\Gamma_{pS}^\ell = \frac{T_s^{v\ell}(\omega)T_s^{\ell b}(\omega)}{\sqrt{\varepsilon_\ell(\omega)}} \left[\frac{t_p^{v\ell}(\omega)t_p^{\ell b}(\omega)}{\varepsilon_\ell(\omega)\sqrt{\varepsilon_b(\omega)}} \right]^2,$$

$$\Gamma_{sP}^\ell = \frac{T_p^{v\ell}(\omega)T_p^{\ell b}(\omega)}{\sqrt{\varepsilon_\ell(\omega)}\varepsilon_\ell(2\omega)\sqrt{\varepsilon_b(2\omega)}} \left[t_s^{v\ell}(\omega)t_s^{\ell b}(\omega) \right]^2,$$

where $\varepsilon_\ell(\omega)$ is the average value of the layer dielectric function, and the $v\ell$ and ℓb superscripts denote either the vacuum-layer or layer-bulk interfaces. The required Fresnel factors are [26]

$$t_p^{\alpha\beta}(\omega) = \frac{2k_\alpha(\omega)\sqrt{\varepsilon_\alpha(\omega)\varepsilon_\beta(\omega)}}{k_\alpha(\omega)\varepsilon_\beta(\omega) + k_\beta(\omega)\varepsilon_\alpha(\omega)},$$

$$t_s^{\alpha\beta}(\omega) = \frac{2k_\alpha(\omega)}{k_\alpha(\omega) + k_\beta(\omega)},$$

where $k_\alpha(\omega) = [\varepsilon_\alpha(\omega) - \sin^2\theta]^{1/2}$ is the magnitude of the wave-vector perpendicular to the surface divided by ω/c, and $\varepsilon_v(\omega) = 1$. The Fresnel factors denoted with capital T can be expressed as $T_i^{\alpha\beta}(\omega) = t_i^{\alpha\beta}(2\omega)$, where i can be either s or p polarization, and $\alpha\beta$ can be either the vacuum-layer or layer-bulk interface. For the remainder of this section, terms represented with capital letters will be evaluated at 2ω. We shall also omit the (ω) and (2ω) dependence on some terms for ease of notation.

The three-layer model described here can be reduced to the two-layer model [26–28], that had been traditionally used to study the SSHG yield. For this reduction, we consider that $\mathcal{P}(2\omega)$ is evaluated in the vacuum region, while the fundamental fields are evaluated in the bulk region. To do this, we take the 2ω radiations factors for vacuum by taking $\ell = v$ [thus $\varepsilon_\ell(2\omega) = 1$, $T_i^{\ell v} = 1$, and $T_i^{\ell b} = T_i^{vb}$] and the fundamental field inside medium b by taking $\ell = b$ [thus $\varepsilon_\ell(\omega) = \varepsilon_b(\omega)$, $t_i^{v\ell} = t_i^{vb}$, and $t_i^{\ell b} = 1$]. This reduces Eq. (2) to the equivalent expression in Refs. [26,27]. Since $\mathcal{P}(2\omega)$ is evaluated in the vacuum we label this model as the two-layer-vacuum model.

A third possibility that we consider is to take both $\mathcal{P}(2\omega)$ and the fundamental fields inside the bulk of the material. The three-layer model can be reduced by taking $\ell = b$, thus $\varepsilon_\ell(2\omega) = \varepsilon_b(2\omega)$, $T_i^{v\ell} = T_i^{b\ell}$, $T_i^{\ell b} = 1$, and $\varepsilon_\ell(\omega) = \varepsilon_b(\omega)$, $t_i^{v\ell} = t_i^{vb}$, and $t_i^{\ell b} = 1$. In this case, $\mathcal{P}(2\omega)$ is evaluated in the bulk, thus we label this model as the two-layer-bulk model. We will compare all three of these models in subsequent sections to determine which one more accurately describes the SSHG yield. We summarize these models in Table I.

The Si(111)(1×1):H surface is in symmetry group C_{3v} and has the following nonzero components [27] of the nonlinear susceptibility tensor, $\chi(-2\omega;\omega,\omega)$:

$$\chi^{zzz} \equiv \chi_{\perp\perp\perp},$$

$$\chi^{zxx} = \chi^{zyy} \equiv \chi_{\perp\parallel\parallel},$$

$$\chi^{xxz} = \chi^{yyz} \equiv \chi_{\parallel\parallel\perp},$$

$$\chi^{xxx} = -\chi^{xyy} = -\chi^{yyx} \equiv \chi_{\parallel\parallel\parallel}.$$

TABLE I. Summary of SSHG yield models. "Label" is the name used in subsequent figures, while the remaining columns show in which medium we will consider the specified quantity. ℓ is the thin layer below the surface of the material, v is the vacuum region, and b is the bulk region of the material. Note that the "vacuum" or "bulk" tag in the label refers to the layer in which $\mathcal{P}(2\omega)$ is evaluated.

Label	$\mathcal{P}(2\omega)$	$\mathbf{E}(\omega)$
Three-layer	ℓ	ℓ
Two-layer-vacuum	v	b
Two-layer-bulk	b	b

We have chosen the x and y axes along the $[11\bar{2}]$ and $[1\bar{1}0]$ directions. The $(-2\omega;\omega,\omega)$ term has been omitted for ease of notation. These tensor components will be given in Sec. III. We are interested in $\mathcal{R}_{pP}$, $\mathcal{R}_{pS}$, and $\mathcal{R}_{sP}$ for our comparison with experiment, so we write the remaining terms of Eq. (2) as

$$r_{pP}^{\ell} = \varepsilon_b(2\omega)\sin\theta\left[\varepsilon_b^2(\omega)\sin^2\theta\,\chi_{\perp\perp\perp} + \varepsilon_\ell^2(\omega)k_b^2\,\chi_{\perp\|\|}\right]$$
$$- \varepsilon_\ell(\omega)\varepsilon_\ell(2\omega)k_b K_b[2\sin\theta\,\varepsilon_b(\omega)\,\chi_{\|\|\perp}$$
$$+ \varepsilon_\ell(\omega)k_b\,\chi_{\|\|\|}\cos 3\phi], \tag{3}$$

$$r_{pS}^{\ell} = -\varepsilon_\ell^2(\omega)k_b^2\,\chi_{\|\|\|}\sin 3\phi, \tag{4}$$

$$r_{sP}^{\ell} = \varepsilon_b(2\omega)\sin\theta\,\chi_{\perp\|\|} + \varepsilon_\ell(2\omega)K_b\,\chi_{\|\|\|}\cos 3\phi. \tag{5}$$

We note that the above treatment is strictly valid within the dipole approximation, and we assume that the bulk quadrupolar SHG response is negligible compared to the dipolar contribution, as reported in the experimental works of Refs. [5,27,29–32]. As such, $\mathcal{R}_{sS} \approx 0$.

III. NONLINEAR SUSCEPTIBILITY TENSOR

Our revised formulation is derived using the length gauge formalism, in the independent particle approximation, and includes (i) the scissors correction, (ii) the contribution of the nonlocal part of the pseudopotential, and (iii) the cut function [20]. We define our electron velocity operator to include these new contributions as

$$\mathbf{v}^\Sigma \equiv \mathbf{v} + \mathbf{v}^{nl} + \mathbf{v}^S \equiv \mathbf{v}^{LDA} + \mathbf{v}^S,$$

with

$$\mathbf{v} = \frac{\mathbf{p}}{m_e}, \quad \mathbf{v}^{nl} = \frac{1}{i\hbar}[\mathbf{r}, V^{nl}],$$

$$\mathbf{v}^S = \frac{1}{i\hbar}[\mathbf{r}, S], \quad \mathbf{v}^{LDA} \equiv \mathbf{v} + \mathbf{v}^{nl},$$

where $\mathbf{p}$ is the momentum operator, m_e is the mass of the electron, $\mathbf{r}$ is the position operator, $\mathbf{v}^{nl}$ is the contribution from the nonlocal part of the pseudopotential (V^{nl}), and $\mathbf{v}^S$ originates from the scissor operator (S).

The approach we use to study the surface of a semi-infinite semiconductor crystal is as follows. Instead of using a semi-infinite system, we replace it with a supercell that consists of a finite slab of atomic layers and a vacuum region. This supercell is repeated to form a full three-dimensional crystalline structure. A convenient way to accomplish the separation of the SH signal of either surface is to introduce a cut function, $\mathcal{C}(z)$, which is usually taken to be unity over one half of the slab and zero over the other half [9]. In this case $\mathcal{C}(z)$ will give the contribution of the side of the slab for which $\mathcal{C}(z) = 1$. We denote this case as the half slab of the material.

Operators denoted with a calligraphic letter are understood to be layered operators that include the cut function, $\mathcal{C}(z)$. We find that all operators can be converted to their calligraphic counterpart as follows [20]:

$$\mathcal{V}^\Sigma = \frac{\mathcal{C}(z)\mathbf{v}^\Sigma + \mathbf{v}^\Sigma \mathcal{C}(z)}{2}.$$

In this way we establish our complete layered velocity operator,

$$\mathcal{V}^\Sigma = \mathcal{V}^{LDA} + \mathcal{V}^S = \mathcal{V} + \mathcal{V}^{nl} + \mathcal{V}^S,$$

which is used to find its matrix elements in the usual way,

$$\mathcal{V}_{mn}^\Sigma(\mathbf{k}) = \int d^3r\,\psi_{m\mathbf{k}}^*(\mathbf{r})\mathcal{V}^\Sigma\psi_{n\mathbf{k}}(\mathbf{r}),$$

where $\psi_{n\mathbf{k}}(\mathbf{r}) = \langle\mathbf{r}|n\mathbf{k}\rangle$ are the real-space representations of the Bloch states $|n\mathbf{k}\rangle$ labeled by the band index n and the crystal momentum $\mathbf{k}$. The band index n can take the value v (c) for valence (conduction) states. The last remaining term is the position operator, which can be calculated directly from the velocity operator,

$$\mathbf{r}_{nm}(\mathbf{k}) = \frac{\mathbf{v}_{nm}^\Sigma(\mathbf{k})}{i\omega_{nm}^\Sigma(\mathbf{k})} = \frac{\mathbf{v}_{nm}^{LDA}(\mathbf{k})}{i\omega_{nm}^{LDA}(\mathbf{k})} \qquad n \notin D_m,$$

where D_m are all the possible degenerate m states. The matrix elements of $\mathbf{r}_{nm}(\mathbf{k})$ are identical using either the local-density approximation (LDA) or scissored Hamiltonian [20], thus negating the need to label them. Of course, it is more convenient to calculate them through $\mathbf{v}_{nm}^{LDA}(\mathbf{k})$, which includes only the contribution of $\mathbf{v}_{nm}^{nl}(\mathbf{k})$.

Using the expressions described above, we write the nonlinear susceptibility tensor in terms of the velocity and position operators as follows [20]:

$$\text{Im}\big[\chi_{e,\omega}^{abc}\big] = \frac{\pi|e|^3}{2\hbar^2}\int\frac{d^3k}{8\pi^3}\sum_{vc}\sum_{q\neq(v,c)}\frac{1}{\omega_{cv}^\Sigma}\left[\frac{\text{Im}\big[\mathcal{V}_{qc}^{\Sigma,a}\{r_{cv}^b r_{vq}^c\}\big]}{(2\omega_{cv}^\Sigma - \omega_{cq}^\Sigma)} - \frac{\text{Im}\big[\mathcal{V}_{vq}^{\Sigma,a}\{r_{qc}^c r_{cv}^b\}\big]}{(2\omega_{cv}^\Sigma - \omega_{qv}^\Sigma)}\right]\delta(\omega_{cv}^\Sigma - \omega), \tag{6a}$$

$$\text{Im}\big[\chi_{i,\omega}^{abc}\big] = \frac{\pi|e|^3}{2\hbar^2}\int\frac{d^3k}{8\pi^3}\sum_{cv}\frac{1}{(\omega_{cv}^\Sigma)^2}\left[\text{Re}\big[\{r_{cv}^b(\mathcal{V}_{vc}^{\Sigma,a})_{;k^c}\}\big] + \frac{\text{Re}\big[\mathcal{V}_{vc}^{\Sigma,a}\{r_{cv}^b\Delta_{cv}^c\}\big]}{\omega_{cv}^\Sigma}\right]\delta(\omega_{cv}^\Sigma - \omega), \tag{6b}$$

$$\text{Im}\big[\chi_{e,2\omega}^{abc}\big] = -\frac{\pi|e|^3}{2\hbar^2} \int \frac{d^3k}{8\pi^3} \sum_{vc} \frac{4}{\omega_{cv}^{\Sigma}} \Bigg[\sum_{v' \neq v} \frac{\text{Im}\big[\mathcal{V}_{vc}^{\Sigma,a}\{r_{cv'}^{b}r_{v'v}^{c}\}\big]}{2\omega_{cv'}^{\Sigma} - \omega_{cv}^{\Sigma}} - \sum_{c' \neq c} \frac{\text{Im}\big[\mathcal{V}_{vc}^{\Sigma,a}\{r_{cc'}^{c}r_{c'v}^{b}\}\big]}{2\omega_{c'v}^{\Sigma} - \omega_{cv}^{\Sigma}} \Bigg] \delta\big(\omega_{cv}^{\Sigma} - 2\omega\big), \tag{6c}$$

$$\text{Im}\big[\chi_{i,2\omega}^{abc}\big] = \frac{\pi|e|^3}{2\hbar^2} \int \frac{d^3k}{8\pi^3} \sum_{vc} \frac{4}{(\omega_{cv}^{\Sigma})^2} \Bigg[\text{Re}\big[\mathcal{V}_{vc}^{\Sigma,a}\{(r_{cv}^{b})_{;k^c}\}\big] - \frac{2\text{Re}\big[\mathcal{V}_{vc}^{\Sigma,a}\{r_{cv}^{b}\Delta_{cv}^{c}\}\big]}{\omega_{cv}^{\Sigma}} \Bigg] \delta\big(\omega_{cv}^{\Sigma} - 2\omega\big), \tag{6d}$$

where $\omega_{nm}^{\Sigma}(\mathbf{k}) \equiv \omega_n^{\Sigma}(\mathbf{k}) - \omega_m^{\Sigma}(\mathbf{k})$. The scissor-shifted energies, $\omega_n^{\Sigma}(\mathbf{k})$, are given by

$$\omega_n^{\Sigma}(\mathbf{k}) = \omega_n^{\text{LDA}}(\mathbf{k}) + (1 - f_n)\Delta,$$

where $\hbar\Delta$ is the rigid (**k**-independent) energy correction to be applied, and f_n is the occupation number of the Bloch state $|n\mathbf{k}\rangle$. These integrals are to be taken over the three-dimensional **k** space. The **k** points are used for the linear analytic tetrahedron method for evaluating the three-dimensional Brillouin-zone integrals [33]. Note that the Brillouin zone for the slab geometry collapses to a two-dimensional zone, with only one **k** point along the z axis. The interband, intraband, 1ω, and 2ω contributions have been split in Eq. (6). The real part of each contribution can be obtained through a Kramers-Kronig transformation [34] and $\chi^{abc}(-2\omega;\omega,\omega) = \chi_{e,\omega}^{abc} + \chi_{e,2\omega}^{abc} + \chi_{i,\omega}^{abc} + \chi_{i,2\omega}^{abc}$. These equations fulfill the required permutation symmetry, so $\chi^{abc} = \chi^{acb}$. The number of atomic layers in the slab must be high enough in order to give converged results for $\chi^{abc}(-2\omega;\omega,\omega)$. If we take $\mathcal{C}(z) = 1$ over the entire slab, the layered matrix elements $\mathcal{V}_{nm}^{\Sigma}$ become bulklike $\mathbf{v}_{nm}^{\Sigma}$ matrix elements, and Eq. (6) is equivalent to the expressions in Ref. [22], valid for bulk semiconductors. As it is mandatory to use $\mathcal{C}(z) = 1$ for one half of the slab, the susceptibility is normalized to the half slab. However, the $\chi^{abc}(-2\omega;\omega,\omega)$ presented in Sec. V are surface susceptibilities normalized to the surface plane. They are then independent of the height of the material slab. Note that the $\chi^{abc}(-2\omega;\omega,\omega)$ components entering in $\mathcal{R}_{iF}$ [Eq. (2)] are always surface susceptibilities, and are calculated in pm^2/V.

We must also calculate the bulk and surface dielectric functions, $\epsilon_b(\omega)$ and $\epsilon_\ell(\omega)$. For this, we follow the method presented in Ref. [35]. For the bulk, the tensor components are equal in all three directions due to the cubic symmetry:

$$\varepsilon_b(\omega) = \epsilon_b^{xx}(\omega) = \epsilon_b^{yy}(\omega) = \epsilon_b^{zz}(\omega).$$

For the purpose of this calculation, we introduce the average value for the surface dielectric function, $\varepsilon_\ell(\omega)$. This entails that $\epsilon_\ell^{xx}(\omega) = \epsilon_\ell^{yy}(\omega) \approx \epsilon_\ell^{zz}(\omega)$, since symmetry is broken in the zz direction because of the surface. We find the average in the conventional way,

$$\varepsilon_\ell(\omega) = \frac{\epsilon_\ell^{xx}(\omega) + \epsilon_\ell^{yy}(\omega) + \epsilon_\ell^{zz}(\omega)}{3},$$

and use that quantity in the equations for the SSHG yield. In order to obtain a result which does not depend on the size of the vacuum region [36], we have normalized the surface dielectric function to the volume of the slab, instead of the volume of the supercell. We remark that we could calculate $\epsilon_{\text{half slab}}^{ab}(\omega)$ using $\mathcal{C}(z) = 1$ for the upper half of our slab and normalize to the

volume of the half slab. Nevertheless, $\epsilon_\ell^{ab}(\omega)$ and $\epsilon_{\text{half slab}}^{ab}(\omega)$ give the same result [36–38].

IV. METHOD

We constructed the Si(111)(1×1):H surface with the experimental lattice constant of 5.43 Å, and then performed structural optimizations with the ABINIT [39,40] code. The structures were relaxed until the Cartesian force components were less than 5 meV/Å, yielding a final Si-H bond distance of 1.50 Å. The energy cutoff used was 20 Ha, and we used Troullier-Martin LDA pseudopotentials [41]. The resulting atomic positions are in good agreement with previous theoretical studies [16,42–45], as well as the experimental value for the Si-H distance [46].

We also evaluated the number of layers required for convergence and settled on a slab with 48 atomic Si planes. The geometric optimizations mentioned above are therefore carried out on slabs of 48 atomic layers without fixing any atoms to the bulk positions. We extract the surface susceptibilities from only half of the slab. This encompasses 24 layers of Si and the single layer of H that terminates the top surface. The vacuum size is equivalent to one-quarter the size of the slab, avoiding the effects produced by possible wave-function tunneling from the contiguous surfaces of the full crystal formed by the repeated supercell scheme [35].

The electronic wave functions, $\psi_{n\mathbf{k}}(\mathbf{r})$, were also calculated with the ABINIT code using a plane-wave basis set with an energy cutoff of 15 hartrees. $\chi^{abc}(-2\omega;\omega,\omega)$ was properly converged with 576 **k** points in the irreducible Brillouin zone, which are equivalent to 1250 **k** points if we disregard symmetry relations. The contribution of $\mathcal{V}^{nl}$ in Eq. (6) was carried out using the DP [47] code with a basis set of 3000 plane waves. Convergence for the number of bands was achieved at 200, which includes 97 occupied bands and 103 unoccupied bands.

All spectra were produced using a scissors value of 0.7 eV in the $\chi^{abc}(-2\omega;\omega,\omega)$ and $\epsilon_\ell(\omega)$ calculations. This value was obtained from Ref. [48], in which the authors carry out a G_0W_0 calculation on this surface for increasing numbers of layers. They calculated the LDA and G_0W_0 band gaps, and found that the difference between the two tends towards ~0.7 eV as more layers are added, culminating in a value of 0.68 eV for bulk Si. This calculation is completely *ab initio*, so we choose 0.7 eV as a very reasonable value for the scissors correction.

Our method of calculation is as follows. We first calculated $\varepsilon_b(\omega)$, $\varepsilon_\ell(\omega)$, and then $\chi^{abc}(-2\omega;\omega,\omega)$ from Eq. (6). We used these for the Fresnel factors and in Eqs. (3)–(5), and finally those into Eq. (2) to obtain the theoretical SSHG yield for different polarizations that can then be compared with the experimental data. All results for $\chi^{abc}(-2\omega;\omega,\omega)$ and $\mathcal{R}_{iF}$ are broadened with a Gaussian broadening with a standard

deviation of $\sigma = 0.075$ eV. This value is chosen such that the theoretical calculation adequately represents the experimental spectrum line shape.

V. RESULTS

In this section, we present our theoretical results compared with the appropriate experimental data. For full details on these experiments, see Refs. [16,21,23,24]. This analysis provides information on the physics behind the SSHG yield and how it is affected by a variety of factors.

A. Calculating $\chi(-2\omega; \omega, \omega)$ using relaxed atomic positions

The pioneering work presented in Ref. [16] showed the effect of artificially moving the atomic position on the resulting SSHG spectra. In this section, we address the more practical and relevant case of atomic relaxation. More precisely, we compare the fully relaxed structure described in Sec. IV with an unrelaxed structure where all the Si atoms are at the ideal bulk positions. Note that in both cases the Si-H bond distance is the same: 1.5 Å.

We compare the calculated $\chi_{\|\|\|\|}(-2\omega; \omega, \omega)$ with experimental data for this surface taken from Ref. [23]. These data provide an excellent point of comparison as they were presented in absolute units and were measured at a very low temperature of 80 K. We used both relaxed (as detailed in Sec. IV) and unrelaxed atomic positions to calculate the nonlinear susceptibility tensor. The calculation with the unrelaxed coordinates was done with the same parameters mentioned above.

We can see from Fig. 2 that the relaxed coordinates have a peak position that is very slightly blueshifted with respect to the experimental peak near 1.7 eV. In contrast, the unrelaxed coordinates have a peak that is redshifted close to 0.05 eV from experiment. There is also a feature between 1.5 and 1.6 eV that appears in the relaxed spectrum that coincides partially with the experimental data. It is important to note that these data were taken at low temperature (80 K); this further favors the comparison, as the theory neglects the effects of temperature. We can also see from Ref. [23] that the peaks in the spectrum
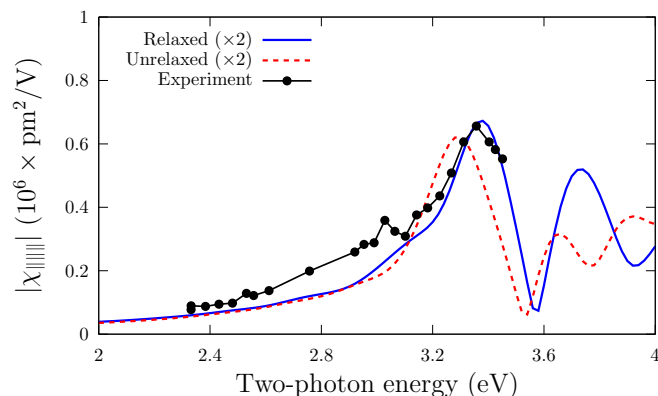
redshift as the temperature increases. Intensity for both the relaxed and unrelaxed curves are roughly half the intensity of the experimental spectrum. We have converted the units of the experimental data from centimeter-gram-second (CGS) to MKS units for easier comparison.

Therefore, the most accurate theoretical results are given by using relaxed atomic positions for the calculation of $\chi(-2\omega; \omega, \omega)$. Although this process can be very time consuming for large numbers of atoms, we consider it a crucial step. From a numerical standpoint, this further demonstrates that SSHG is very sensitive to the surface atomic positions. In particular, our results show that a correct value of the Si-H bond length is not enough to obtain the most accurate SSHG spectra, and that a full relaxation of the structure is required. Additionally, the theory may coincide better with experiments that are conducted under very low-temperature conditions.

B. Calculated $\mathcal{R}_{pS}$ compared to experiment

All calculations presented from this point on were done using the relaxed atomic positions described in previous sections. We now move on to the theoretical SSHG yield compared with experiment. We first compare the calculated $\mathcal{R}_{pS}$ spectra with room-temperature experimental data from Ref. [16]. We adhere to the experimental setup by taking an angle of incidence $\theta = 65°$ and an azimuthal angle of $\phi = 30°$ with respect to the x axis. This azimuthal angle maximizes r_{pS}, as shown in Eq. (4). In Fig. 3, we see that all three models reproduce the line shape of the experimental spectrum which includes the peaks corresponding to both the E_1 (3.4 eV) and E_2 (4.3 eV) critical points of bulk silicon, and a smaller feature at around 3.8 eV. The calculated E_1 and E_2 peaks are redshifted by 0.1 and 0.06 eV, respectively, compared with the experimental peaks.

The main issue to address here is the discrepancy between the intensity of the E_1 peak. In the theoretical curves, the peaks differ only slightly in overall intensity. Conversely, the experimental E_1 peak is significantly smaller than the E_2 peak. This may be due to the effects of oxidation on the surface. Reference [24] features similar data to those of Ref. [16] but
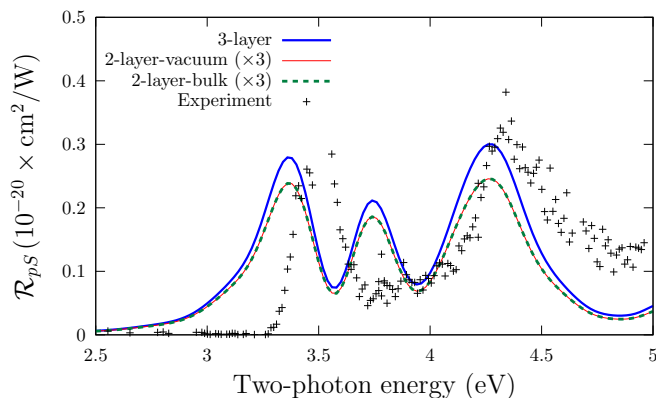

FIG. 2. Comparison of $\chi_{\|\|\|\|}(-2\omega; \omega, \omega)$ calculated using relaxed and unrelaxed atomic positions, with the experimental data presented in Ref. [23]. Theoretical curves are broadened with $\sigma = 0.075$ eV. Experimental data were taken at 80 K.

FIG. 3. Comparison between theoretical models (see Table I) and experiment for $\mathcal{R}_{pS}$, for $\theta = 65°$. We use a scissors value of $\hbar\Delta = 0.7$ eV. All theoretical curves are broadened with $\sigma = 0.075$ eV. Experimental data are taken from Ref. [16], measured at room temperature.
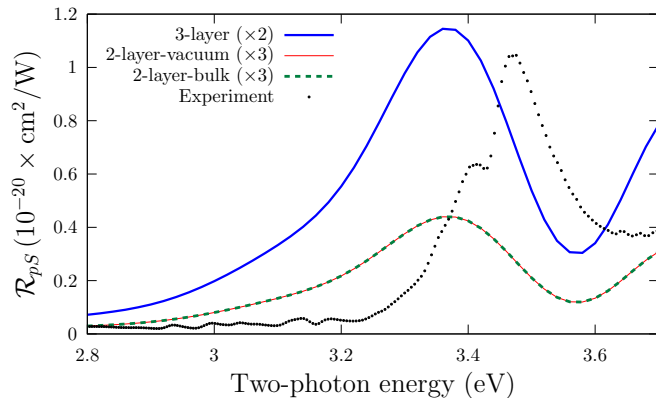
FIG. 4. Comparison between theoretical models (see Table I) and experiment for $\mathcal{R}_{pS}$, for $\theta = 45°$. We use a scissors value of $\hbar\Delta = 0.7\,\text{eV}$. All theoretical curves are broadened with $\sigma = 0.075\,\text{eV}$. Experimental data are taken from Ref. [21], measured at room temperature.
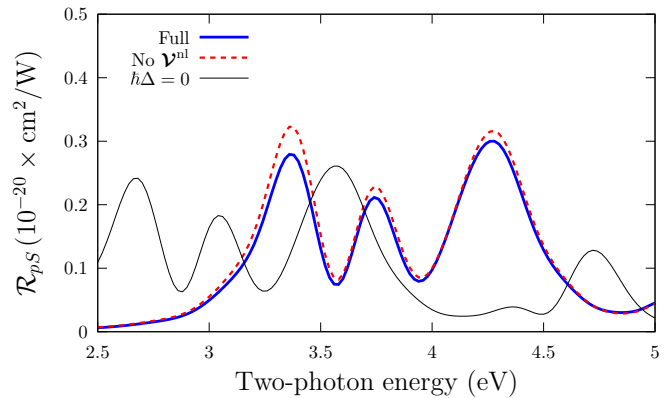

FIG. 5. Calculated results for $\mathcal{R}_{pS}$ for the different levels of approximation proposed in this paper. All curves were calculated using the three-layer model. We take $\theta = 65°$ for this plot. See text for full details. All curves are broadened with $\sigma = 0.075\,\text{eV}$.

focuses on the effects of surface oxidation. We can see that as time passes during the experiment the surface becomes more oxidized, and the E_1 peak diminishes substantially, as shown by the experimental data taken 5 h after initial H termination. This may be enough time to slightly reduce the E_1 peak intensity, as can be observed here.

In Fig. 4, we compare the theoretical $\mathcal{R}_{pS}$ with experimental data from Ref. [21]; these data, however, only encompass the E_1 peaks and were obtained at room temperature. We consider an angle of incidence $\theta = 45°$ and an azimuthal angle $\phi = 30°$ to match these experimental conditions. As in the previous comparison, the E_1 peak is slightly redshifted compared to experiment. The intensity of the theoretical yield is smaller than the experimental yield for all three models. The measurements presented in Ref. [21] were taken very shortly after the surface had been prepared, and the surface itself was prepared with a high degree of quality and measured at room temperature. Peak position compared to theory is slightly improved under these conditions. As before, the three-layer model is closer in intensity to the experimental spectrum.

We show in Fig. 2 that our calculation for $\chi_{\parallel\parallel\parallel}(-2\omega;\omega,\omega)$ coincides with the measurement taken at a low temperature of 80 K. It is well known that temperature causes shifting in the peak position of SSHG spectra [49]. As $\mathcal{R}_{pS}$ only depends on this component [see Eq. (4)], the position of the theoretical peak should be correct in Figs. 3 and 4. We deduce that the difference in peak position stems from the higher temperature at which the experiments were measured.

Both the two-layer-vacuum and two-layer-bulk models are identical and roughly three times smaller than the experiment. We can see from Eq. (4) that $\mathcal{R}_{pS}$ only has 1ω terms [$\varepsilon_\ell(\omega)$ and k_b]. For both of these models, the fundamental fields are evaluated in the bulk, which means that the only change to Eq. (4) is that $\varepsilon_\ell(\omega) \to \varepsilon_b(\omega)$. Additionally, Γ_{pS}^ℓ also remains identical between the two models and has no 2ω terms in the denominator. Therefore, r_{pS} is identical between these two models. Ultimately, the intensity of the three-layer model is the closest to the experiment.

Per Eq. (4), the intensity of $\mathcal{R}_{pS}$ depends only on $\chi_{\parallel\parallel\parallel}$, which is not affected by local-field effects [50]. These effects

are neglected in this calculation, but $\mathcal{R}_{pS}$ maintains an accurate line shape and provides a good quantitative description of the experimental SSHG yield. We note that both the calculated and experimental spectra show two-photon resonances at the energies corresponding to the critical point transitions of bulk Si. We also see that the SSHG yield drops rapidly to zero below E_1, which is consistent with the absence of surface states due to the H saturation on the surface. This observation holds true for all three polarization cases studied here.

Lastly, in Fig. 5 we provide an overview of the different levels of approximation proposed in this paper. All curves here were calculated using the three-layer model. The long dashed line depicts the effect of excluding the contribution from the nonlocal part of the pseudopotentials. This is consistent with the results reported in Ref. [20], where the exclusion of this term increases the intensity of the components of $\boldsymbol{\chi}(-2\omega;\omega,\omega)$ by approximately 15 to 20%. We also notice that the E_1 peak is larger than the E_2 peak, contrasting with the experiment, where the E_1 peak is smaller than E_2. Lastly, the thin solid line depicts the full calculation with a scissors value of $\hbar\Delta = 0$. We notice that the spectrum is almost rigidly redshifted as this H-saturated surface has no electronic surface states [20]. Thus, this demonstrates the importance of including the scissors correction to accurately reproduce the experimental spectrum. In summary, the inclusion of the contribution from the nonlocal part of the pseudopotentials and the scissors operator on top of the three-layer model produces spectra with a line shape and intensity that compare favorably with the experimental data.

C. Calculated $\mathcal{R}_{sP}$ compared to experiment

Next, we analyze and compare the calculated $\mathcal{R}_{sP}$ spectra with experimental data from Ref. [16]. We again adhere to the experimental setup by taking an angle of incidence $\theta = 65°$ and an azimuthal angle $\phi = 30°$. From Fig. 6, we can immediately appreciate that the overall intensity of $\mathcal{R}_{sP}$ is one order of magnitude lower than $\mathcal{R}_{pS}$. The experimental data are far noisier than in the other cases but we can still discern the E_1 and E_2 peaks. As with our previous comparisons, the three-layer model is the closest match in both intensity and line shape to the experimental spectrum. It produces a curve that is
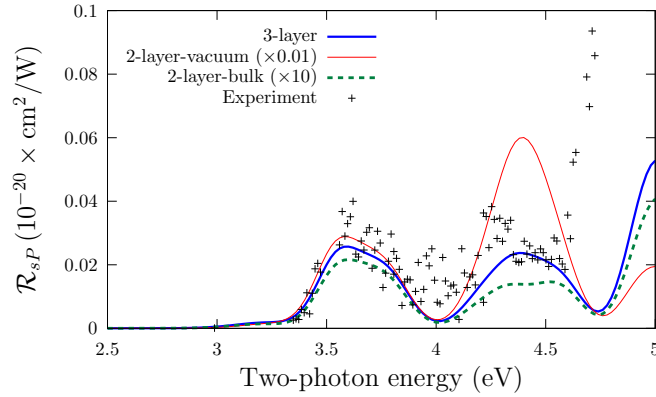
FIG. 6. Comparison between theoretical models (see Table I) and experiment for $\mathcal{R}_{sP}$, for $\theta = 65°$. We use a scissors value of $\hbar\Delta = 0.7$ eV. All theoretical curves are broadened with $\sigma = 0.075$ eV. Experimental data are taken from Ref. [16], measured at room temperature.

FIG. 7. Comparison between theoretical models (see Table I) and experiment for $\mathcal{R}_{pP}$, for $\theta = 65°$. We use a scissors value of $\hbar\Delta = 0.7$ eV. All theoretical curves are broadened with $\sigma = 0.075$ eV. Experimental data are taken from Ref. [16], measured at room temperature.

very close to the experimental intensity with good proportional heights for the calculated E_1 and E_2 peaks. In contrast, the two-layer-vacuum model is 100 times more intense than experiment and produces an enlarged E_2 peak. The two-layer-bulk model is ten times smaller with a very similar line shape to the three-layer model.

The differences between the two-layer-vacuum and two-layer-bulk models are not derived from Eq. (5), as the $\varepsilon_b(2\omega)$ does not change and the second term vanishes for this azimuthal angle of $\phi = 30$. However, Γ^ℓ_{sP} does cause a significant change in the intensity as there is an $\varepsilon_\ell(2\omega)$ term in the denominator. This will become $\varepsilon_v(2\omega) = 1$ for the two-layer-vacuum model, and $\varepsilon_b(2\omega)$ in the bulk model. This accounts for the significant difference between the intensity of the two models, while the line shape remains mostly consistent.

At higher energies, the theoretical curve is blueshifted as compared to the experiment. We consider that the likely explanation for this is the inclusion of the scissor operator, which does not adequately correct the transitions occurring at these higher energies. A full *GW* calculation would be well suited for this task, but is beyond the scope of this paper.

D. Calculated $\mathcal{R}_{pP}$ compared to experiment

We present $\mathcal{R}_{pP}$ compared to experimental data from Ref. [16] in Fig. 7. We note that peak position for the three-layer model is similar to experiment with the overall intensity being only two times larger. The E_2 peak is blueshifted by around 0.3 eV, and the yield does not go to zero after 4.75 eV. The two-layer-vacuum model produces a spectrum with peak positions that are close to the experiment, but are 40 times more intense. The calculated E_2 peak is similar, but the E_1 peak lacks the sharpness present in the experiment. The two-layer-bulk model is very close to the line shape of the three-layer model, but with eight times less intensity. From Eq. (3), we see that $\mathcal{R}_{pP}$ has several 2ω terms that will change between models; this will have a deep effect on the line shape. Additionally, Γ^ℓ_{pP} also has $\varepsilon_\ell(2\omega)$ in the denominator, and so we have a significant difference in both line shape and intensity between the two-layer-vacuum and the other two models. Again, as in
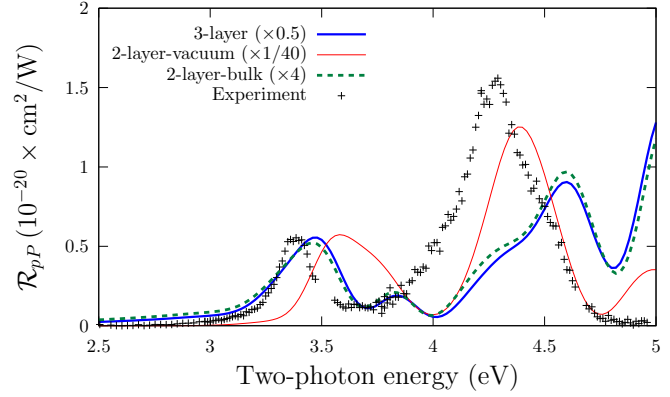
the previous sections for $\mathcal{R}_{pS}$ and $\mathcal{R}_{sP}$, the three-layer model is the closest in intensity to the experiment. Additionally, Ref. [49] shows that low-temperature measurements of $\mathcal{R}_{pP}$ will blueshift the spectrum away from room-temperature measurements such as those shown in Figs. 7 and 8, and towards our theoretical results.

Reviewing Eq. (3), we see that $\mathcal{R}_{pP}$ is by far the most involved calculation, since it includes all four nonzero components. In particular, $\chi_{\perp\perp\perp}$ and $\chi_{\parallel\parallel\perp}$ include out-of-plane incoming fields. These are affected by local-field effects [50], that reveal the inhomogeneities in the material, which are by far more prevalent perpendicular to the surface than in the surface plane. This can be evidenced for Si, as reflectance anisotropy spectroscopy measurements are well described by *ab initio* calculations neglecting local-field effects [51,52]. It is therefore expected that the out-of-plane components will be more sensitive to the inclusion of local fields. These will not change the transition energies, only their relative weights of the resonant peaks [50], but including these effects is
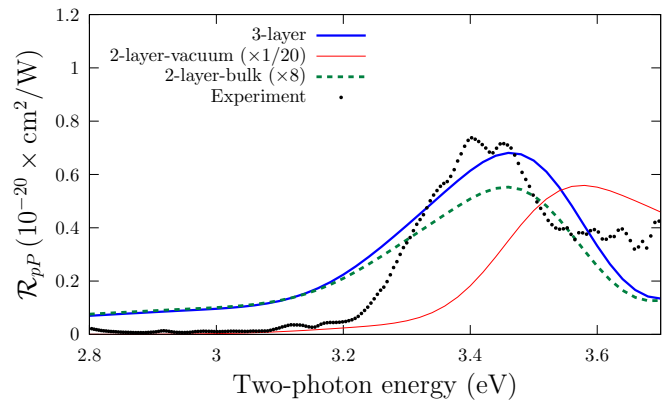

FIG. 8. Comparison between theoretical models (see Table I) and experiment for $\mathcal{R}_{pP}$, for $\theta = 45°$. We use a scissors value of $\hbar\Delta = 0.7$ eV. All theoretical curves are broadened with $\sigma = 0.075$ eV. Experimental data are taken from Ref. [21], measured at room temperature.

challenging to compute [36], and beyond the scope of this paper. We speculate that $\mathcal{R}_{pP}$ requires the proper inclusion of these effects in order to accurately describe the experimental peaks.

In Fig. 8 we compare to Ref. [21]. The three-layer model is, as before, close to the experiment in both peak position and intensity. Intensity is almost the same as the experimental value. This provides a more compelling argument against the two-layer-vacuum model than Fig. 7. The two-layer-vacuum model is 20 times more intense and blueshifted by around 0.1 eV. As mentioned before, this surface is of very high quality with measurements taken shortly after surface preparation. As before, the two-layer-bulk model is intermediate between the other two models in both intensity and line shape. Under these conditions, the three-layer model very accurately reproduces the E_1 peak over the two-layer-vacuum and two-layer-bulk models.

Lastly, for linear optics and SHG, GW transition energies are needed. Doing a Bethe-Salpeter calculation for SSHG will improve the position and the amplitude of the peaks, but is far beyond current capabilities [53]. We did not adjust the value of the scissors shift, as we want to keep our calculation at the *ab initio* level. We remark again that the choice of $\hbar\Delta = 0.7$ eV for the scissors shift comes from a GW calculation [48]. As explained in Fig. 5, the lack of surface states causes an almost rigid shift of the spectra by applying the scissors correction. We have checked that it is not possible to have a single scissors value that can reproduce the energy positions of both the E_1 and the E_2 peaks. Of course, the experimental temperature at which the spectra is measured should be taken into account in a more complete formulation. However, we have restricted our calculation to $T = 0$ K.

VI. CONCLUSIONS

We have presented *ab initio* LDA calculations for SSHG that are in good quantitative agreement with experimental SSHG spectra for the Si(111)(1×1):H surface. These calculations include contributions not previously considered in a single formulation, to wit, (i) the scissors correction, (ii) the contribution of the nonlocal part of the pseudopotentials, and (iii) the cut function used to extract the surface response, all within the independent particle approximation. We also revised the three-layer model for the SSHG yield where the nonlinear polarization, $\mathcal{P}(2\omega)$, and the fundamental fields

are taken within a small layer ℓ below the surface of the material. This model reproduces key spectral features and yields an intensity closer to the experiment for all cases of $\mathcal{R}_{iF}$. We consider it an upgrade over the much reviewed two-layer model [26], and it comes with very little added computational expense. Additionally, we have compared these two models with another definition of the two-layer model, where both $\mathcal{P}(2\omega)$ and the fundamental fields are considered inside the bulk of the material. We found that this model yields an intensity lower than the three-layer model, but far closer than the two-layer-vacuum model. Line shape is very similar between the three-layer and two-layer-bulk models. Therefore, we consider that the three-layer model offers the closest comparison to experiment, while the two-layer-bulk model offers a reasonable compromise between the three-layer and two-layer-vacuum models.

This study affords us an interesting view of both the theoretical and experimental aspects of SSHG studies. On the theoretical side, we have shown the importance of using relaxed atomic positions to more accurately calculate the nonlinear susceptibility tensor. The intensity of these spectra is greatly improved when compared to previous works [16]. We also postulate that the lack of local-field effects in the theory is a serious shortcoming, but in this case it only affects two of the $\boldsymbol{\chi}(-2\omega;\omega,\omega)$ components.

Concerning the experiments, we show that surface preparation and quality are important for better results. The approach for calculating the SSHG yield presented here finds closer agreement with surfaces that are freshly prepared with little or no oxidation, and with measurements taken at low temperatures.

Overall, this framework for calculating $\boldsymbol{\chi}(-2\omega;\omega,\omega)$ and $\mathcal{R}$ focused on the well-known Si(111)(1×1):H surface provides a compelling benchmark for SSHG studies. We are confident that this work can be applied directly to many other surfaces of interest.

[1] N. Bloembergen, Appl. Phys. B **68**, 289 (1999).

[2] C. K. Chen, A. R. B. de Castro, and Y. R. Shen, Phys. Rev. Lett. **46**, 145 (1981).

[3] W. Daum, H. J. Krause, U. Reichel, and H. Ibach, Phys. Rev. Lett. **71**, 1234 (1993).

[4] M. C. Downer, Y. Jiang, D. Lim, L. Mantese, P. T. Wilson, B. S. Mendoza, and V. Gavrilenko, Phys. Status Solidi A **188**, 1371 (2001).

[5] M. C. Downer, B. S. Mendoza, and V. I. Gavrilenko, Surf. Interface Anal. **31**, 966 (2001).

[6] J. L. P. Hughes and J. E. Sipe, Phys. Rev. B **53**, 10751 (1996).

[7] J. F. McGilp, M. Cavanagh, J. R. Power, and J. D. O'Mahony, Opt. Eng. **33**, 3895 (1994).

[8] J. F. McGilp, Surf. Rev. Lett. **6**, 529 (1999).

[9] B. S. Mendoza, A. Gaggiotti, and R. Del Sole, Phys. Rev. Lett. **81**, 3781 (1998).

[10] Y. R. Shen, Nature (London) **337**, 519 (1989).

[11] J. J. Dean, C. Lange, and H. M. van Driel, Phys. Rev. B **89**, 024102 (2014).

[12] L. M. Malard, T. V. Alencar, Ana Paula M. Barboza, K. F. Mak, and A. M. de Paula, Phys. Rev. B **87**, 201401 (2013).

[13] Z. H. Levine, Phys. Rev. B **49**, 4532 (1994).

[14] N. Arzate and B. S. Mendoza, Phys. Rev. B **63**, 125303 (2001).

[15] B. S. Mendoza, M. Palummo, G. Onida, and R. Del Sole, Phys. Rev. B **63**, 205406 (2001).

[16] J. E. Mejía, B. S. Mendoza, M. Palummo, G. Onida, R. Del Sole, S. Bergfeld, and W. Daum, Phys. Rev. B **66**, 195329 (2002).

[17] H. Sano, G. Mizutani, W. Wolf, and R. Podloucky, Phys. Rev. B **66**, 195338 (2002).

[18] J. E. Mejía, C. Salazar, and B. S. Mendoza, Revista Mexicana de Física **50**, 134 (2004).

[19] M. L. Trolle, G. Seifert, and T. G. Pedersen, Phys. Rev. B **89**, 235410 (2014).

[20] S. M. Anderson, N. Tancogne-Dejean, B. S. Mendoza, and V. Véniard, Phys. Rev. B **91**, 075302 (2015).

[21] S. A. Mitchell, M. Mehendale, D. M. Villeneuve, and R. Boukherroub, Surf. Sci. **488**, 367 (2001).

[22] J. L. Cabellos, B. S. Mendoza, M. A. Escobar, F. Nastos, and J. E. Sipe, Phys. Rev. B **80**, 155205 (2009).

[23] U. Höfer, Appl. Phys. A **63**, 533 (1996).

[24] S. Bergfeld, B. Braunschweig, and W. Daum, Phys. Rev. Lett. **93**, 097402 (2004).

[25] S. M. Anderson and B. S. Mendoza, arXiv:1604.07722 (2016).

[26] V. Mizrahi and J. E. Sipe, J. Opt. Soc. Am. B **5**, 660 (1988).

[27] J. E. Sipe, D. J. Moss, and H. M. van Driel, Phys. Rev. B **35**, 1129 (1987).

[28] N. Bloembergen and P. S. Pershan, Phys. Rev. **128**, 606 (1962).

[29] O. A. Aktsipetrov, I. M. Baranova, and Yu. A. Il'inskii, Zh. Eksp. Teor. Fiz. **91**, 287 (1986) [J. Exp. Theor. Phys. **64**, 167 (1986)].

[30] Z. Xu, X. F. Hu, D. Lim, J. G. Ekerdt, and M. C. Downer, J. Vac. Sci. Technol. B **15**, 1059 (1997).

[31] P. Guyot-Sionnest and Y. R. Shen, Phys. Rev. B **38**, 7985 (1988).

[32] Y. R. Shen, Appl. Phys. B **68**, 295 (1999).

[33] F. Nastos, B. Olejnik, K. Schwarz, and J. E. Sipe, Phys. Rev. B **72**, 045223 (2005).

[34] N. Tancogne-Dejean, B. S. Mendoza, and V. Véniard, Phys. Rev. B **90**, 035212 (2014).

[35] B. S. Mendoza, F. Nastos, N. Arzate, and J. E. Sipe, Phys. Rev. B **74**, 075318 (2006).

[36] N. Tancogne-Dejean, C. Giorgetti, and V. Véniard, Phys. Rev. B **92**, 245308 (2015).

[37] C. Hogan, R. Del Sole, and G. Onida, Phys. Rev. B **68**, 035405 (2003).

[38] C. Castillo, B. S. Mendoza, W. G. Schmidt, P. H. Hahn, and F. Bechstedt, Phys. Rev. B **68**, 041310 (2003).

[39] X. Gonze, B. Amadon, P. M. Anglade, J. M. Beuken, F. Bottin, P. Boulanger, F. Bruneval, D. Caliste, R. Caracas, M. Cote *et al.*, Comput. Phys. Commun. **180**, 2582 (2009).

[40] The ABINIT code is a common project of the Université Catholique de Louvain, Corning, Inc., and other contributors (http://www.abinit.org).

[41] N. Troullier and J. L. Martins, Phys. Rev. B **43**, 1993 (1991).

[42] E. Kaxiras and J. D. Joannopoulos, Phys. Rev. B **37**, 8842 (1988).

[43] F. Jona, W. A. Thompson, and P. M. Marcus, Phys. Rev. B **52**, 8226 (1995).

[44] D. R. Alfonso, C. Noguez, D. A. Drabold, and S. E. Ulloa, Phys. Rev. B **54**, 8028 (1996).

[45] F. Cargnoni, C. Gatti, E. May, and D. Narducci, J. Chem. Phys. **112**, 887 (2000).

[46] R. C. Weast, M. J. Astle, and W. H. Beyer, *CRC Handbook of Chemistry and Physics* (CRC, Boca Raton, 1988), Vol. 69.

[47] V. Olevano, L. Reining, and F. Sottile, http://dp-code.org.

[48] Y. Li and G. Galli, Phys. Rev. B **82**, 045321 (2010).

[49] J. I. Dadap, Z. Xu, X. F. Hu, M. C. Downer, N. M. Russell, J. G. Ekerdt, and O. A. Aktsipetrov, Phys. Rev. B **56**, 13367 (1997).

[50] N. Tancogne-Dejean, Ph.D. thesis, Ecole Polytechnique, 2015, https://pastel.archives-ouvertes.fr/tel-01235611.

[51] M. Palummo, G. Onida, R. Del Sole, and B. S. Mendoza, Phys. Rev. B **60**, 2522 (1999).

[52] K. Gaál-Nagy, A. Incze, G. Onida, Y. Borensztein, N. Witkowski, O. Pluchery, F. Fuchs, F. Bechstedt, and R. Del Sole, Phys. Rev. B **79**, 045312 (2009).

[53] The size of the excitonic Hamiltonian scales as $(N_k^3 \times N_v \times N_c)^2$, where N_k is the total number of **k** points, and N_v and N_c are the number of valence and conduction states, respectively. For these values, the size of the Hamiltonian for the Si(111)(1×1):H surface of this paper would be over 1 petabyte, which far exceeds conventional computing capabilities.